Magnetic resonance lymphography at 9.4 T using a gadolinium-based nanoparticle in rats: investigations in healthy animals and in a hindlimb lymphedema model

Müller, Andreas ; Fries, Peter ; Jelvani, Bijan ; Lux, François ; Rübe, Claudia E ; Kremp, Stephanie ; Giovanoli, Pietro ; Buecker, Arno ; Menger, Michael D ; Laschke, Matthias W ; Frueh, Florian S

Abstract: OBJECTIVES: Magnetic resonance lymphography (MRL) in small animals is a promising but challenging tool in preclinical lymphatic research. In this study, we compared the gadolinium (Gd)-based nanoparticle AGuIX with Gd-DOTA for interstitial MRL in healthy rats and in a chronic rat hindlimb lymphedema model. MATERIALS AND METHODS: A comparative study with AGuIX and Gd-DOTA for interstitial MRL was performed in healthy Lewis rats (n = 6). For this purpose, 75 L of 3 mM AGuIX (containing 30 mM Gd-DOTA side residues) and 75 L 30 mM Gd-DOTA were injected simultaneously in the right and left hindlimbs. Repetitive high-resolution, 3-dimensional time-of-flight gradient recalled echo MRL sequences were acquired over a period of 90 minutes using a 9.4 T animal scanner. Gadofosveset-enhanced MR angiography and surgical dissection after methylene blue injection served as supportive imaging techniques. In a subsequent proof-of-principle study, AGuIX-based MRL was investigated in a hindlimb model of chronic lymphedema (n = 4). Lymphedema of the right hindlimbs was induced by means of popliteal and inguinal lymphadenectomy and irradiation with 20 Gy. The nonoperated left hindlimbs served as intraindividual controls. Six, 10, and 14 weeks after lymphadenectomy, MRL investigations were performed to objectify lymphatic reorganization. Finally, skin samples of the lymphedematous and the contralateral control hindlimbs were analyzed by means of histology and immunohistochemistry. RESULTS: AGuIX-based MRL resulted in high-resolution anatomical depiction of the rodent hindlimb lymphatic system. Signal-to-noise ratio and contrast-to-noise ratio of the popliteal lymph node were increased directly after injection and remained significantly elevated for up to 90 minutes after application. AGuIX provided significantly higher and prolonged signal intensity enhancement as compared with Gd-DOTA. Furthermore, AGuIX-based MRL demonstrated lymphatic regeneration in the histopathologically verified chronic lymphedema model. Collateral lymphatic vessels were detectable 6 weeks after lymphadenectomy. CONCLUSIONS: This study demonstrates that AGuIX is a suitable contrast agent for preclinical interstitial MRL in rodents. AGuIX yields anatomical imaging of lymphatic vessels with diameters greater than 200 m. Moreover, it resides in the lymphatic system for a prolonged time. AGuIX may therefore facilitate high-resolution MRL-based analyses of the lymphatic system in rodents.

DOI: https://doi.org/10.1097/RLI.0000000000000398

Originally published at:
Müller, Andreas; Fries, Peter; Jelvani, Bijan; Lux, François; Rübe, Claudia E; Kremp, Stephanie; Giovanoli, Pietro; Buecker, Arno; Menger, Michael D; Laschke, Matthias W; Frueh, Florian S (2017). Magnetic resonance lymphography at 9.4 T using a gadolinium-based nanoparticle in rats: investigations in healthy animals and in a hindlimb lymphedema model. Investigative Radiology, 52(12):725-733.
DOI: https://doi.org/10.1097/RLI.0000000000000398

Magnetic Resonance Lymphography at 9.4 T Using a Gadolinium-Based Nanoparticle in Rats

Investigations in Healthy Animals and in a Hindlimb Lymphedema Model

Andreas Müller, PhD, Peter Fries, MD,* Bijan Jelvani,† François Lux, PhD,‡ Claudia E. Rübe, MD,§ Stephanie Kremp, MSc,§ Pietro Giovanoli, MD,|| Arno Buecker, MD,* Michael D. Menger, MD,† Matthias W. Laschke, MD, PhD,† and Florian S. Frueh, MD†||*

Objectives: Magnetic resonance lymphography (MRL) in small animals is a promising but challenging tool in preclinical lymphatic research. In this study, we compared the gadolinium (Gd)-based nanoparticle AGuIX with Gd-DOTA for interstitial MRL in healthy rats and in a chronic rat hindlimb lymphedema model.

Materials and Methods: A comparative study with AGuIX and Gd-DOTA for interstitial MRL was performed in healthy Lewis rats (n = 6). For this purpose, 75 μL of 3 mM AGuIX (containing 30 mM Gd-DOTA side residues) and 75 μL 30 mM Gd-DOTA were injected simultaneously in the right and left hindlimbs. Repetitive high-resolution, 3-dimensional time-of-flight gradient recalled echo MRL sequences were acquired over a period of 90 minutes using a 9.4 T animal scanner. Gadofosveset-enhanced MR angiography and surgical dissection after methylene blue injection served as supportive imaging techniques. In a subsequent proof-of-principle study, AGuIX-based MRL was investigated in a hindlimb model of chronic lymphedema (n = 4). Lymphedema of the right hindlimbs was induced by means of popliteal and inguinal lymphadenectomy and irradiation with 20 Gy. The nonoperated left hindlimbs served as intraindividual controls. Six, 10, and 14 weeks after lymphadenectomy, MRL investigations were performed to objectify lymphatic reorganization. Finally, skin samples of the lymphedematous and the contralateral control hindlimbs were analyzed by means of histology and immunohistochemistry.

Results: AGuIX-based MRL resulted in high-resolution anatomical depiction of the rodent hindlimb lymphatic system. Signal-to-noise ratio and contrast-to-noise ratio of the popliteal lymph node were increased directly after injection and remained significantly elevated for up to 90 minutes after application. AGuIX provided significantly higher and prolonged signal intensity enhancement as compared with Gd-DOTA. Furthermore, AGuIX-based MRL demonstrated lymphatic regeneration in the histopathologically verified chronic lymphedema model. Collateral lymphatic vessels were detectable 6 weeks after lymphadenectomy.

Conclusions: This study demonstrates that AGuIX is a suitable contrast agent for preclinical interstitial MRL in rodents. AGuIX yields anatomical imaging of lymphatic vessels with diameters greater than 200 μm. Moreover, it resides in the lymphatic system for a prolonged time. AGuIX may therefore facilitate high-resolution MRL-based analyses of the lymphatic system in rodents.

Key Words: AGuIX, lymphangiography, lymphatic imaging, lymph node enhancement, magnetic resonance lymphography, polysiloxane nanoparticle, small animal lymphography

(*Invest Radiol* 2017;52: 725–733)

Lymphatic imaging is an emerging field in preclinical research. It has been overshadowed for long by angiogenesis research because high-resolution imaging techniques were not available for the lymphatic vasculature.[1] Direct lymphography in small animals is difficult, and intralymphatic cannulation is not suitable for repetitive in vivo analyses.[2] Hence, interstitial contrast deposition with transport through lymphatic capillaries represents the logical solution. Several techniques have been established for interstitial lymphography in small animals, such as fluorescence microlymphography,[3] magnetic resonance lymphography (MRL),[4,5] and near-infrared fluorescence lymphography.[6,7] In contrast to fluorescence-based lymphography, interstitial MRL is not limited by superficial penetration depth and yields information on tissue quality (ie, fibrosis, fatty deposits). Besides lymphatic vessel imaging, it allows additional lymph node characterization and staging.[8]

Interstitial MRL in animals has been performed with different contrast agents. These include gadolinium (Gd)-labeled dendrimers,[9,10] macrocyclic Gd-complexes,[4,11–13] Gd-labeled dextran,[14] and hepatobiliary contrast agents.[15] However, the translation of these macromolecules into clinical application is restricted by delayed renal clearance and uptake into the reticulo-endothelial system. Furthermore, interstitial MRL with commercially available extracellular Gd-chelates is markedly limited by nonspecific distribution.[12] Hence, an ongoing need exists for contrast agents with better suitability for preclinical and clinical MRL.

The Gd-based nanoparticle AGuIX has been proposed for theranostic applications including different imaging modalities and anatomical localizations.[16] The concept of detection and radiotherapy of malignant brain and lung tumors has been investigated in laboratory animals.[17–19] Intravenously applied AGuIX is currently under clinical investigation serving as a radiosensitizer for the treatment of brain metastases. Based on previous studies on pharmacodynamic and pharmacokinetic properties, we hypothesized that AGuIX might be particularly suited for interstitial MRL. For verification, we herein performed a comparative study with Gd-DOTA in healthy rats. Gadofosveset-based MR angiography served as a control experiment to illustrate the vascular system. In a subsequent proof-of-principle study, MRL investigations with interstitial AGuIX application were performed in a chronic lymphedema model of the rat hindlimb.

Received for publication April 3, 2017; and accepted for publication, after revision, May 23, 2017.

From the *Clinic of Diagnostic and Interventional Radiology, Saarland University Medical Center, Homburg/Saar, Germany; †Institute for Clinical and Experimental Surgery, Saarland University, Homburg/Saar, Germany; ‡Institut Lumière Matière, Université Claude Bernard Lyon 1, CNRS, Lyon, France; §Department of Radiotherapy and Radiation Oncology, Saarland University Medical Center, Homburg/Saar, Germany; and ||Division of Plastic Surgery and Hand Surgery, University Hospital Zürich, University of Zürich, Zürich, Switzerland.

Conflicts of interest and sources of funding: F.L. has 1 patent to disclose (WO 2011135101). This patent protects the nanoparticles described in this publication (AGuIX). F.L. is also cofounder of NH TherAguix Society that has the exclusive license for the AGuIX nanoparticles. F.S.F. received support from the Deutsche Gesellschaft für Lymphologie (DGL, grant number Fo0315), S&T AG Microsurgical Instruments (Neuhausen, Switzerland), and the Gesellschaft Deutschsprachiger Lymphologen (GDL). For the remaining authors, none were declared.

Correspondence to: Florian S. Frueh, MD, Institute for Clinical and Experimental Surgery, Saarland University, Kirrbergerstrasse, Building 65, 66421 Homburg/Saar, Germany; and Division for Plastic Surgery and Hand Surgery, University Hospital Zürich, Rämistrasse 100, 8091 Zürich, Switzerland. E-mail: florian.frueh@usz.ch.

ISSN: 0020-9996/17/5212–0725
DOI: 10.1097/RLI.0000000000000398

MATERIALS AND METHODS

Contrast Agents

AGuIX has been described previously in detail.[16] In brief, it consists of 10 Gd-DOTA species binding to a polysiloxane core. Compared with other nanoparticles, it has a rather small molecular mass of 8.5 ± 1.0 kDa with a mean hydrodynamic diameter of 3.0 ± 1.0 nm. The molecule size and the rigid structure yield substantial MR contrast enhancement with higher r1 relaxivities than for free Gd-DOTA.[20] Solutions were prepared freshly for each animal from dry substance at a concentration of 3 mM AGuIX, 145 mM NaCl, 2 mM $CaCl_2 \cdot 6\ H_20$, 5 mM HEPES, pH 7.4 from a sterile filtrated stock solution and sterile pure water (Aqua ad iniectabilia; B. Braun Melsungen AG, Melsungen, Germany). At a concentration of 3 mM, the nanoparticle solution contained 30 mM Gd-DOTA side residues.

Gd-DOTA (Dotarem; Guerbet, Aulnay-sous-Bois, France) served as control contrast agent. Gd-DOTA is clinically approved by the Food and Drug Administration for intravenous use with MR imaging in the brain (intracranial), spine, and associated tissues in adult and pediatric patients. Imaging properties of this agent in MRL have previously been characterized in different animal studies.[21,22] The Gd-DOTA stock solution supplied at 500 mM was diluted to a concentration of 30 mM with sterile pure water. Subsequently, equal doses of Gd were applied with the corresponding contrast agents for the MR experiment.

For MRL, the fourth phalanx of both hindlimbs was injected intradermally with 75 μL of the contrast medium preparations using a 31-gauge syringe (Hamilton Bonaduz AG, Bonaduz, Switzerland).

For contrast-enhanced MR angiography, gadofosveset (Vasovist; Bayer, Leverkusen, Germany) was applied as an intravenous bolus injection at a dose of 0.2 mL/kg, equaling 0.03 mmol/kg body weight, as described previously.[23] Gadofosveset binds reversibly to endogenous serum albumin, resulting in a longer vascular residence time and a higher r1 relaxivity with an increase in blood vessel signal intensity (SI).

Animals

All experiments were performed with 3- to 4-month-old male Lewis rats (Janvier Labs, Le Genest-Saint-Isle, France) exhibiting a mean body weight of 390 ± 40 g. The animals were housed one per cage under a 12-hour day/night cycle and were fed ad libitum with water and standard pellet food (Altromin, Lage, Germany). All experiments were conducted in accordance with the European legislation on the protection of animals (Directive 2010/63/EU) and the National Institutes of Health guidelines on the care and use of laboratory animals (National Institutes of Health publication #85-23 Rev. 1985) and were approved by the local governmental animal care committee (permission number: 67/2015).

Experimental Protocol

In 6 healthy animals, a comparative study with simultaneous intradermal injection of AGulX in the right and Gd-DOTA in the left hindlimb was conducted. After contrast application, 6 repetitive MRL scans were performed. After MRL completion, gadofosveset was applied via a tail vein catheter, and MR angiography studies were performed. Finally, methylene blue was injected intradermally, the animals were killed, and the lymphatic system of the hindlimb was dissected under a stereomicroscope for illustration purposes.

In 4 animals, we investigated AGulX for lymphatic imaging in a chronic lymphedema model. Lymphedema was induced by means of popliteal and inguinal lymphadenectomy with subsequent irradiation. Magnetic resonance lymphography investigations were performed 6, 10, and 14 weeks after lymphadenectomy. After the last scan, the animals were killed and tissue specimens were processed for histological and immunohistochemical analyses.

Magnetic Resonance Imaging

Animals were examined in a horizontal-bore 9.4 T animal scanner (BioSpec Avance III 94/20; Bruker Biospin GmbH, Ettlingen, Germany) with a BGA12S gradient system (maximum field strength, 675 $mT \cdot m^{-1}$; linear inductive rise time, 130 microseconds; maximum slew rate, 4673 mT/m per second) run with ParaVision 6.0.1 (Bruker Biospin GmbH). All animals were placed in supine position and transferred to the magnet tail-first. Imaging was performed using a linearly polarized coil developed for imaging of the rat abdomen with an inner diameter of 72 mm (Bruker Biospin GmbH). Imaging was performed in coronal orientation with a 3-dimensional (3D) gradient recalled echo (GRE) time-of-flight (TOF) sequence adjusted to the blood flow velocity. Because of the low flow velocities experienced perpendicular to the *z* axis, this approach led to a reduction of the SI from blood vessels in the hindlimbs. Finally, MR angiography was performed using a 3D GRE sequence with field of view and matrix settings identical to MRL. Scan duration was 14 minutes and 36 seconds for MRL and 15 minutes and 52 seconds for angiography sequences. Details of the sequence parameters are given in Table 1.

MRL Data Processing and Analysis

Acquired image data were transferred to an external workstation. Multiplanar reconstruction in coronal, axial, and sagittal orientation, 3D maximum intensity projection, and quantitative analyses of 2-dimensional coronal MR images were performed with the 32-bit OsiriX v.4.1.2 software (Pixmeo Sarl, Bernex, Switzerland). For the 6 animals of the comparative study, lymph node enhancement after AGuIX and Gd-DOTA injection was quantified. For determination of signal-to-noise ratio (SNR), the entire popliteal lymph nodes were segmented manually by regions of interest (ROI). The resulting SIs on unenhanced and contrast-enhanced images were recorded and averages per lymph node and time point were calculated thereof. In addition, SI of the muscle tissue adjacent to the lymph node was assessed on the basis of ROI measurements. Noise was measured as average standard deviation (SD) of the background signal collected from 2 identically sized ROIs placed independently in the air next to the animals. Signal-to-noise ratio for each time point investigated was determined as follows:

$$SNR_{LNseg} = \text{Mean } SI_{LN} / \text{Mean } SD_{background}.$$

From the SI data recorded for the segmented lymph nodes and adjacent muscle, highest SI values were extracted (SI_{Lnmax}; $SI_{musclemax}$),

TABLE 1. Detailed MR Imaging Sequence Parameters

Sequence	Purpose	TR, ms	TE, ms	Flip Angle, degree	FOV, mm	Matrix	Voxel Size, μm	Zero Fill	NA
2D-GRE	Localizer	10.0	2.50	10	100 × 100	150 × 150	667 × 667 × 1000	1 × 1	1
3D-TOF-GRE	Lymphography	10.0	2.50	40	80 × 70 × 40	600 × 528 × 300	133 × 133 × 133	2 × 2 × 2	2
3D-GRE	Angiography	10.8	2.95	7.5	80 × 70 × 40	600 × 528 × 300	133 × 133 × 133	2 × 2 × 2	2

MR indicates magnetic resonance; TR, repetition time; TE, echo time; FOV, field of view; NA, number of averages; 2D, 2-dimensional; GRE, gradient recalled echo; 3D, 3-dimensional; TOF, time-of-flight.

and maximum SNR for the popliteal lymph nodes and adjacent muscle of each animal per time point were calculated as:

$$\mathrm{SNR_{LNmax}} = \mathrm{SI_{LNmax}}/\mathrm{Mean\ SD_{background}}.$$

$$\mathrm{SNR_{musclemax}} = \mathrm{SI}_{musclemax}/\mathrm{Mean\ SD_{background}}.$$

For determination of maximum contrast-to-noise ratio ($\mathrm{CNR_{LNmax}}$), ROIs were placed in muscle tissue next to the lymph nodes investigated, and the highest SI within the ROIs were recorded. Corresponding $\mathrm{CNR_{LNmax}}$ was calculated as follows:

$$\mathrm{CNR_{LNmax}} = \mathrm{SI_{LNmax}} - \mathrm{SI_{musclemax}}/\mathrm{Mean\ SD_{background}}.$$

Maximum lymph node–to–muscle ratio (LN/muscle ratio) was calculated as:

$$\mathrm{LN/muscle\ ratio} = \mathrm{SNR_{LNmax}}/\mathrm{SNR_{musclemax}}.$$

Lymphedema Animal Model

Chronic lymphedema was established by combined surgical and radiation ablation of the lymphatic system in right hindlimbs.[24] The nonoperated left hindlimbs served as intraindividual controls.

Surgery

Rats were anesthetized by intraperitoneal injection of ketamine (80 mg/kg body weight; Ursotamin; Serumwerk Bernburg AG, Bernburg, Germany) and xylazine (6 mg/kg body weight; Rompun; Bayer, Leverkusen, Germany). After depilation of the right hindlimb, the animals were placed on an operation stage, kept warm with an infrared lamp, and the right paw was injected intradermally with 0.1 mL methylene blue 10% (Carl Roth GmbH, Karlsruhe, Germany). The collecting lymphatic vessels of the hindlimb were ligated microsurgically before piercing the biceps femoris (Fig. 1A), and popliteal (Fig. 1B) as well as inguinal fat pads were resected. Incisions were closed with 5/0 monofilament (Prolene; Ethicon, Johnson & Johnson Medical GmbH, Norderstedt, Germany). Postoperative analgesia was provided with subcutaneous buprenorphine (0.05 mg/kg body weight; Buprenovet; Bayer Vital GmbH, Leverkusen, Germany) and tramadol hydrochloride for 3 days (40 mg per 100 mL drinking water; Tramal; Grünenthal GmbH, Aachen, Germany). Wound healing and animal behavior were checked regularly.

Irradiation

For planning, a representative rat was scanned with a computed tomography scanner (Brilliance CT Big Bore; Philips Healthcare, Eindhoven, the Netherlands). The scan parameters were defined as 120-kV voltage, 450 mA with pixel spacing of 0.10 mm, and slice thickness of 0.75 mm. This planning data set was used to define the planning target volume (PTV) in the right groin (Fig. 1C), and the treatment plan was calculated using the Pinnacle v9.8 planning system (Philips Healthcare). The PTV was expanded 6 mm and planned with a single 6-MV photon multileaf collimator field from anterior direction (Fig. 1D). The dose grid was 1 × 1 × 1 mm and the prescribed dose was 20 Gy in a depth of 25 mm (Fig. 1E). The mean dose in the PTV was 19.1 ± 1.1 Gy. The animals were irradiated 2 weeks after surgery.

Paw Thickness Measurements

Caliper-measured paw thickness represents a valid surrogate parameter for rodent hindlimb volumes.[25] Repetitive measurements in isoflurane anesthesia were performed over a period of 14 weeks.

Histology and Immunohistochemistry

Skin samples were fixed in 4% formalin, embedded in paraffin, and cut into 3-µm thick sections. Individual sections were stained with hematoxylin and eosin according to standard procedures. Using a BX60 microscope (Olympus, Hamburg, Germany) and the imaging software

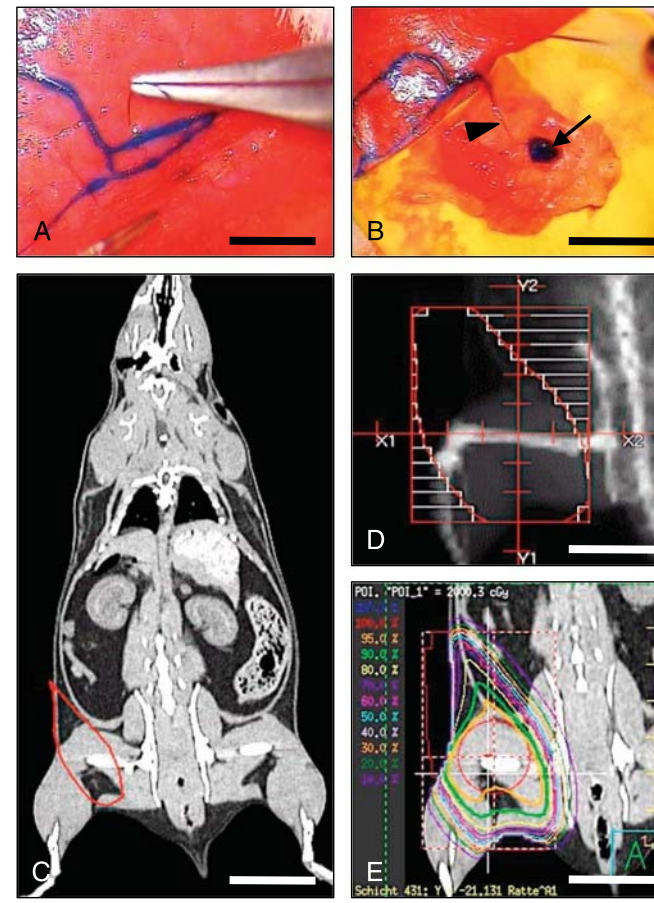

FIGURE 1. Animal model. A, Microsurgical ligation of lymphatic vessels. B, Popliteal lymphadenectomy with lymph node (arrow) and afferent lymphatic vessels (arrowhead). C, Coronal computed tomography image for irradiation planning of the right groin (red circle indicates planning target volume). D, Digitally reconstructed radiograph with multileaf collimator field used for irradiation. E, Coronal computed tomography image with isodose lines illustrating the dose distribution. Scale bars: A = 3.5 mm, B = 6 mm, C = 22 mm, D = 12 mm, E = 19 mm.

cellSens Dimension 1.11 (Olympus), epidermal thickness was assessed. For blinding purposes, a grid was applied, individual values were evaluated in 4 randomized ROIs per section, and average epidermal thickness was calculated. To evaluate the collagen density, additional sections were stained with Sirius red. Under polarized light, mature collagen fibers (type I) appear reddish due to birefringence.[26] The collagen content was assessed in 6 randomized ROIs per section. Individual thresholding was used to calculate the Sirius red–positive tissue fraction.

To quantify immune cell infiltration, sections were stained with a polyclonal rabbit antibody against CD68 (1:50; ab125212, Abcam, Cambridge, United Kingdom) and a polyclonal rabbit antibody against CD3 (1:100; ab166609, Abcam) followed by a biotinylated goat anti–rabbit IgG antibody (ready-to-use; Abcam). The biotinylated antibody was detected by peroxidase-labeled streptavidin (1:50; Sigma-Aldrich, Taufkirchen, Germany). 3-Amino-9-ethylcarbazole (Abcam) was used as chromogen. Cell infiltration was quantified in 10 randomized ROIs per section using the software package ImageJ.[27]

For immunohistochemical analyses of lymphatic vessels, additional sections were stained with a polyclonal rabbit antibody against lymphatic vessel endothelial hyaluronan receptor-1 (LYVE-1) (1:600; ab14917, Abcam). A goat anti–rabbit IgG Alexa555 antibody (1:200; Life Technologies, Eugene, OR) served as secondary antibody. Cell

nuclei were stained with bisbenzimide (1:500; Hoechst 33342, Sigma-Aldrich) for exact image merging. Quantitative analyses of 6 randomized ROIs per section were performed with ImageJ and included the determination of lymphatic vessel density and lymphatic vessel area.

Statistics

Data were analyzed for normal distribution and equal variance. Two groups were compared using the paired *t* test (parametric data) or the Wilcoxon signed rank test (nonparametric data). To test for time effects within groups, analysis of variance for repeated measurements (parametric data) or the Friedman test (nonparametric data) were applied followed by the Dunnett post hoc test. Data are given as mean ± standard deviation unless otherwise indicated. Dot plots are shown with the median as single line and the interquartile range (IQR, 25% to 75% data range) as continuous line. For box plots, the box includes the IQR and the whiskers illustrate at most 1.5 times the IQR. The horizontal line represents the median and an open dot represents the mean. Statistical significance was accepted for $P < 0.05$. Statistical analyses were performed with SigmaPlot (Systat Software Inc, San Jose, CA) and R (R Core Team, Vienna, Austria).[28]

RESULTS

MRL in Healthy Animals

Lymphangiography

With the selected MR imaging strategies, both lymphatic and blood vessels of the rat hindlimb could be clearly discriminated (Fig. 2). Magnetic resonance lymphography performed directly after AGuIX application allowed high-resolution depiction of the lymphatic vessel anatomy in vivo correlating to ex vivo hindlimb dissection after methylene blue injection (Fig. 2, B, D, and E). The collecting lymphatic vessels were characterized by a typical appearance with varying diameter and strong contrast enhancement, whereas veins appeared smoother and less pronounced (Fig. 2, B and C). Efferent lymphatic vessels (Fig. 2, B, F, and G) exhibited a tortuous course toward the inguinal region.

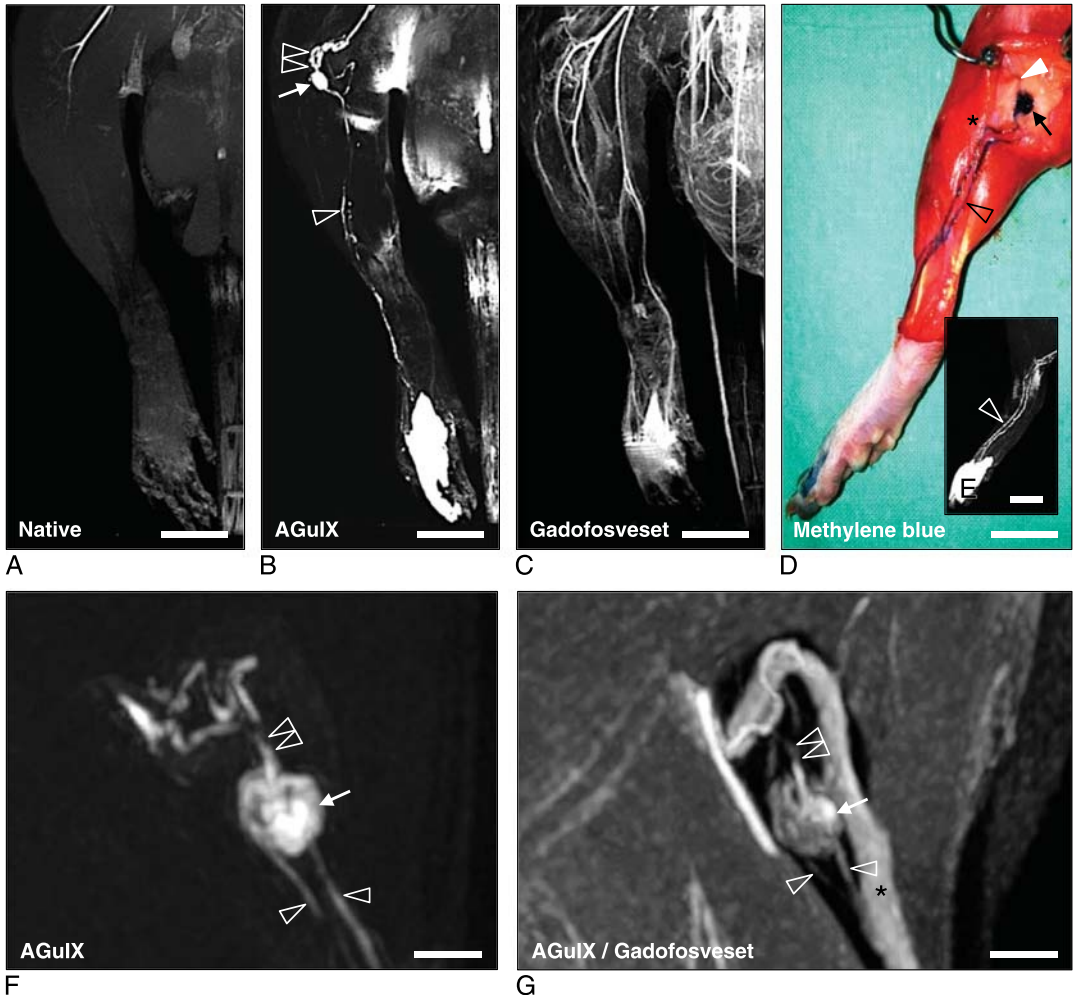

FIGURE 2. MRL and MR angiography in healthy rats. A and B, 3D-TOF-GRE hindlimb scan before (A) and after (B) intradermal AGuIX injection. B, Afferent lymphatic vessels (arrowhead) draining to the popliteal lymph node (arrow). Double arrowhead indicates efferent lymphatic vessel. C, 3D-GRE angiography with intravenous gadofosveset ~120 minutes after AGuIX application. D, Anatomical dissection after methylene blue injection. Afferent lymphatic vessels (arrowhead) piercing the fascia of the biceps femoris (asterisk). Arrow indicates popliteal lymph node. White arrowhead indicates vascular lymph node pedicle. E, Corresponding dorsolateral view of the paw after AGuIX injection with the collecting lymphatic vessels (arrowhead). F, MRL with detailed anatomy of the 2 afferent lymphatic vessels (arrowheads), the lymph node (arrow), and the efferent lymphatic vessel (double arrowhead). G, Additional angiography reveals close vicinity of the short saphenous vein (asterisk). Scale bars: A–D = 8 mm, E = 6.5 mm, F and G = 1.75 mm.

Signal intensity of lymphatic vessels decreased over time, but typical characteristics were preserved (Fig. 3). Afferent and efferent lymphatic vessels remained delineable up to 60 minutes after AGuIX injection. In MRL scans performed 75 and 90 minutes after administration, residual traces of the contrast medium could be detected in the lymphatic vessels with a substantial amount of AGuIX retained in the popliteal lymph node as well as at the injection site (Fig. 3, E and F). In contrast, Gd-DOTA injection resulted in contrasting of veins, afferent and efferent lymphatic vessels 15 minutes after contrast application (Fig. 3A). Initial contrast enhancement was stronger for the short saphenous vein than for the afferent lymphatic vessels. Venous contrast enhancement was reduced 30 minutes after administration, and lymphatic vessel imaging was improved at this time point (Fig. 3B). However, lymphatic vessel delineation was markedly enhanced in AGuIX-injected hindlimbs, whereas Gd-DOTA was completely cleared from the injection site after 90 minutes (Fig. 3F).

Lymphadenography

AGuIX and Gd-DOTA injections resulted in an early peak enhancement of the popliteal lymph node 15 minutes after injection (Figs. 3, 4) with a continuous washout throughout the 90-minute observation period. AGuIX SNR_{LNseg} was significantly higher compared with Gd-DOTA for all experimental time points (Fig. 4G). AGuIX injection resulted in a 7.3-fold increase in mean SNR_{LNseg} from 9.5 ± 1.9 to 68.7 ± 14.1. Ninety minutes after administration, mean SNR_{LNseg} still remained 2.7 times higher than initially recorded. In contrast, Gd-DOTA injection was associated with a SNR_{LNseg} increase by a factor of 3.7 from 10.2 ± 2.1 to 37.7 ± 7.4. Furthermore, mean SNR_{LNseg} in the Gd-DOTA group dropped to baseline already 60 minutes after administration. SNR_{LNmax} measurements revealed an 11.5-fold increase in the AGuIX group from 19.9 ± 4.0 to 229.0 ± 72.5 (Fig. 4H). Ninety minutes after administration, SNR_{LNmax} still remained significantly elevated when compared with preinjection values. For Gd-DOTA injected hindlimbs, SNR_{LNmax} rose 7.0-fold from 20.3 ± 4.0 to 142.0 ± 48.2 and returned to baseline level as early as 45 minutes after application.

Accordingly, CNR_{LNmax} in the AGuIX group exhibited a 28.5-fold increase from 7.6 ± 3.3 before application to 216 ± 68.6 15 minutes after injection (Fig. 4I). However, 60 minutes after contrast application, no significant difference to baseline was detectable. Gd-DOTA injection led to a CNR_{LNmax} increase by a factor of 17.2, from 6.5 ± 1.9 to 117.9 ± 49.9 with return to baseline level 45 minutes after application.

Furthermore, LN/muscle ratio after AGuIX injection showed a 9.7-fold increase from 1.5 ± 0.2 before application to 14.4 ± 4.0 15 minutes after application (Fig. 4J). Injection of Gd-DOTA led to a 6.2-fold increase of LN/muscle ratio from 1.4 ± 0.2 to 8.9 ± 3.3 with reduction to baseline level 45 minutes after administration.

Characterization of Chronic Hindlimb Lymphedema in Rats

All incisions healed uneventfully. Combined surgical and radiation ablation of the lymphatic system resulted in increased hindlimb volumes as indicated by paw thickness measurements (Fig. 5A). Accordingly, the epidermal layer of the groin skin was significantly thicker in the lymphedema group (Fig. 5, B–D). Moreover, histological and immunohistochemical analyses revealed typical hallmarks of chronic lymphedema, such as tissue fibrosis (Fig. 5, E–G), immune cell infiltration (Fig. 5, H–K), and increased density and dilatation of lymphatic vessels (Fig. 5, L–O).

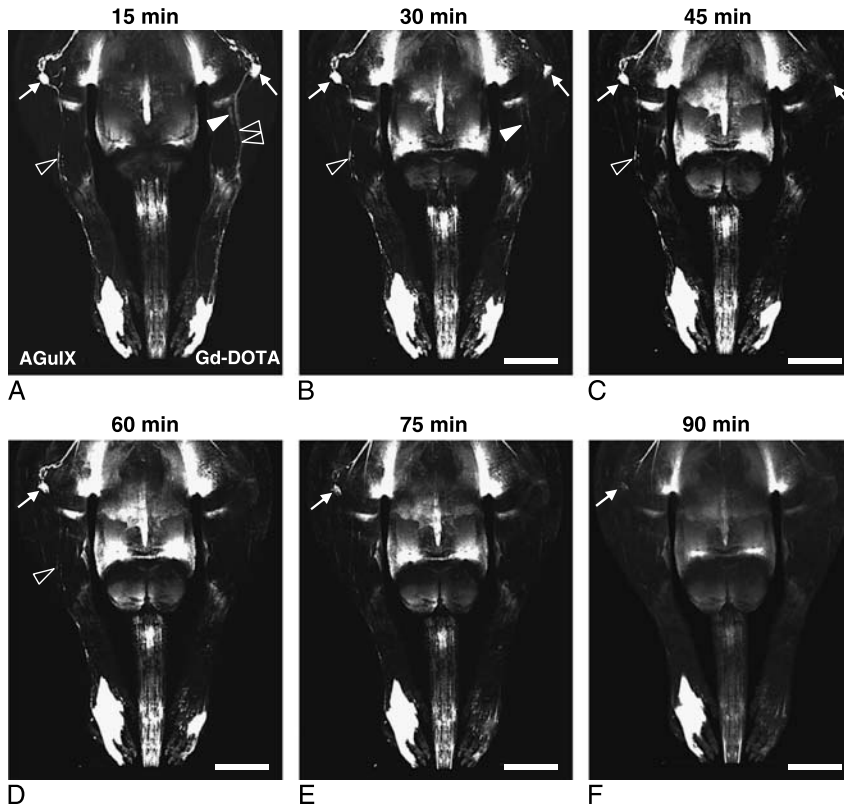

FIGURE 3. 3D-TOF-GRE MRL with AGuIX and Gd-DOTA. A, Selective AGuIX uptake into the collecting lymphatic vessels (arrowhead). Gd-DOTA injection primarily results in contrasting the short saphenous vein (double arrowhead) with minor lymphatic vessel enhancement (white arrowhead). B–F, Repetitive imaging illustrates quick Gd-DOTA washout from the injection site. Arrow indicates popliteal lymph node. Scale bars: 9.5 mm.

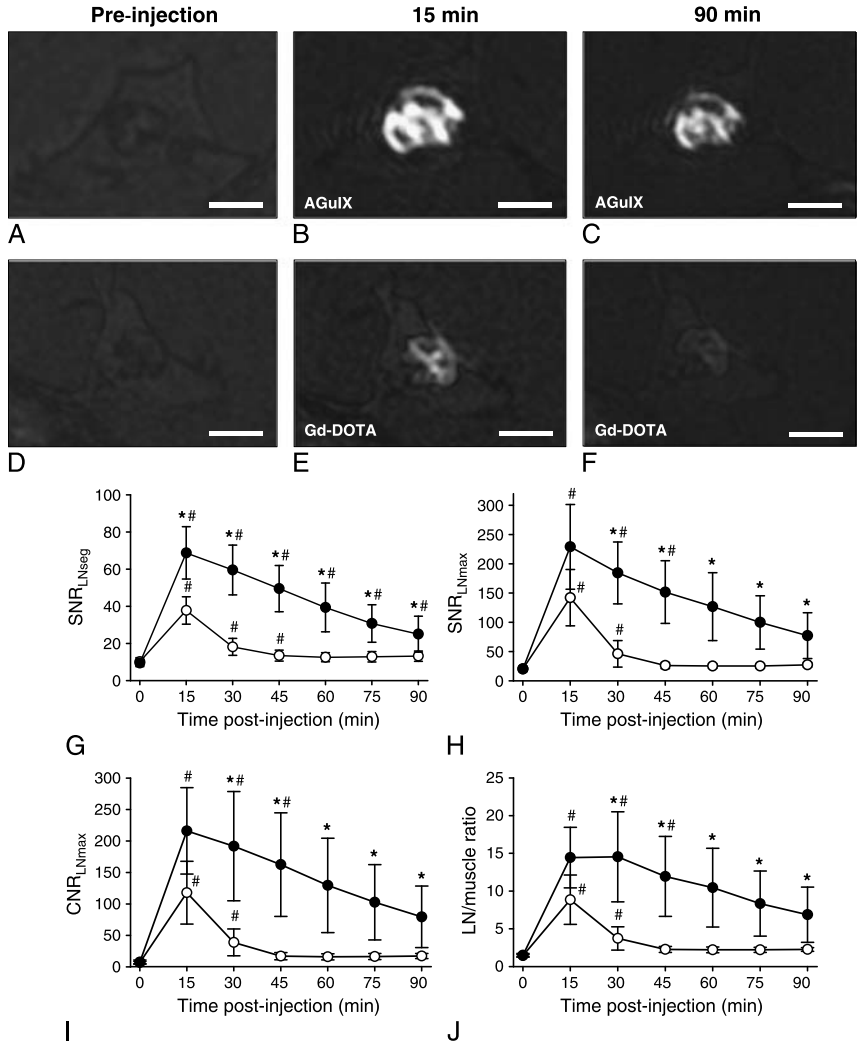

FIGURE 4. Effects of AGuIX and Gd-DOTA on popliteal lymph node contrast. A–F, Coronal 3D-TOF-GRE scans before (A and D), 15 minutes (B and E), and 90 minutes (C and F) after simultaneous application of AGuIX and Gd-DOTA. Scale bars: A–F = 1.5 mm. G–J, Nanoparticle-based MRL (black circles) results in significantly increased SNR_{LNseg} (G), SNR_{LNmax} (H), CNR_{LNmax} (I), and LN/muscle ratio (J) when compared with Gd-DOTA (white circles). Measurements are given in arbitrary units. Mean ± standard deviation, n = 6, $^{*}P < 0.05$ vs Gd-DOTA, $^{\#}P < 0.05$ vs 0 minute.

MRL in Chronic Hindlimb Lymphedema

Six weeks after lymphedema induction, multiple collateral lymphatic vessels draining toward the inguinal ligament were detectable, as illustrated by AGuIX-based MRL (Fig. 6A). These newly visualized lymphatic vessels exhibited a different morphology with a higher variation in diameter. Accordingly, lymphatic reorganization on the dorsum of the paws after 6 weeks was characterized by a dense reticular network from which the new collateral lymphatic vessels originated (Fig. 6D). At this time, residual dermal backflow was present around the ligated lymphatic vessels (Fig. 6, E and F) as compared with nonoperated control hindlimbs (Fig. 6, G–I). However, subsequent MRL investigations 10 and 14 weeks after surgery showed a decrease of collateral lymphatic vessels (Fig. 6, B and C).

DISCUSSION

Magnetic resonance imaging of the lymphatic system exhibits several advantages. It has higher temporal and spatial resolution than radionuclide labeling and is suited for detailed 3D investigation of lymphatic vessels with a diameter in the submillimeter range. In the clinical setting, MRL has already been applied for detection of metastases that have segregated to sentinel lymph nodes,[29,30] or for diagnosing lymphatic vessel abnormalities.[31] However, many MRL methods have not been translated from preclinical or clinical research to standard procedures for patients and contrast agents applied for this purpose are not clinically approved[29,30] or used off-label.[31]

In this study, we evaluated the investigational nanoparticle AGuIX for MRL in rats. Besides relaxivity (r1 and r2), the size of the nanoparticles of the contrast agent and its weight and lipophilicity are the factors that crucially determine pharmacodynamic and pharmacokinetic properties in vivo. Accordingly, Kobayashi et al[9] demonstrated that transport with lymphatic vessels, lymph node enhancement, and elimination from the lymphatic system are correlated to the size of the contrast agent. Larger particles cause strong and long-lasting contrast enhancement in lymph nodes, whereas small molecules are eliminated quickly. The pharmacokinetic properties of AGuIX fit well within these results. At a molecular weight of 8.5 kDa, AGuIX exhibits slowed transit through the lymphatic system. In fact, mean SNR of the popliteal lymph node remained significantly increased up to 90 minutes after AGuIX injection.

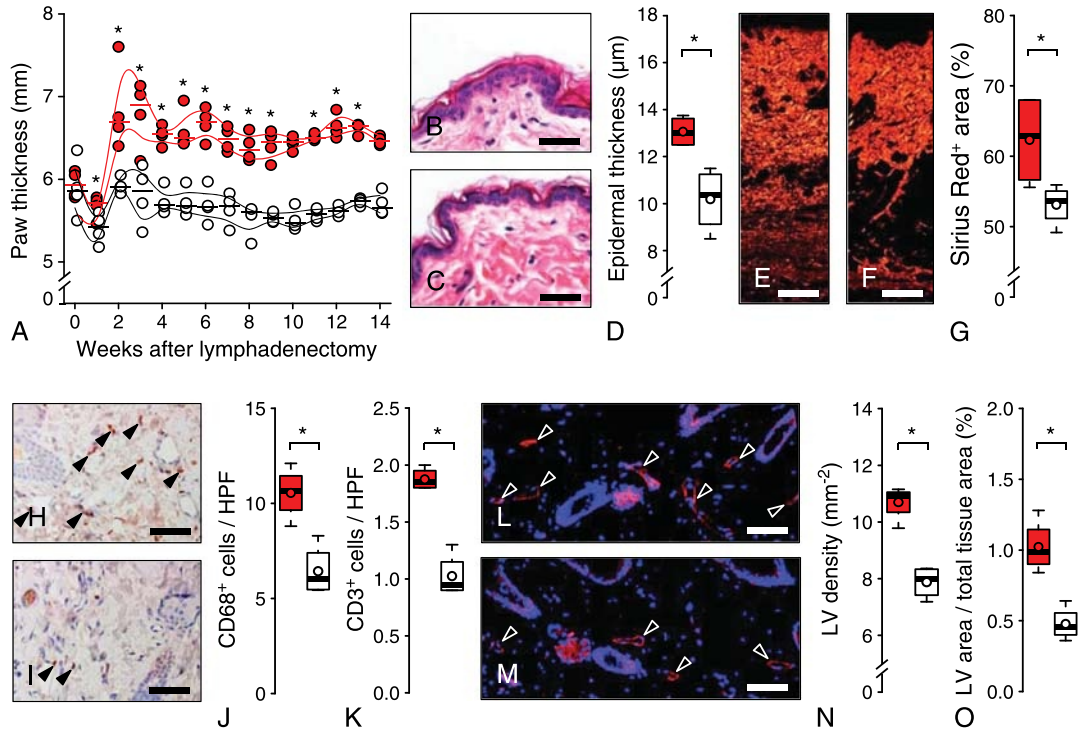

FIGURE 5. Characterization of chronic hindlimb lymphedema in rats. A, Paw thickness of lymphedematous (red dots) and control (white dots) hindlimbs. B and C, Hematoxylin and eosin–stained groin skin samples of lymphedematous (B) and control (C) hindlimbs. D, Increased epidermal thickness in the lymphedema (red box plots) compared with the control group (white box plots). E–G, Sirius red–stained groin sections of lymphedematous (E and G; red box plots) and control (F and G; white box plots) hindlimbs reveals significant tissue fibrosis. H–K, Paw skin samples of lymphedematous (H) and control (I) hindlimbs with $CD68^+$ macrophages (black arrowheads). Both macrophages (J) and $CD3^+$ T-lymphocytes (K) are significantly increased in the lymphedema (red box plots) compared with the control group (white box plots). HPF indicates high-power field. L–O, LYVE-1–stained sections of lymphedematous (L) and control (M) hindlimbs with higher lymphatic vessel (LV, arrowheads) density and area in the lymphedema (N and O; red box plots) compared with the control group (white box plots). Nuclei are stained with bisbenzimide (blue): n = 4, $*P < 0.05$ vs control (white plots). Scale bars: B and C = 40 µm, E and F = 220 µm, H and I = 60 µm, L and M = 145 µm.

Based on its larger hydrodynamic diameter and higher mass as compared with Gd-DOTA, AGuIX showed a limited transit from the interstitium into venous vessels and was predominantly drained from the injection site via lymphatic vessels. This effect could be visualized up to 60 minutes after injection. In contrast to the MRL studies performed with AGuIX, Gd-DOTA application primarily resulted in simultaneous enhancement of the short saphenous vein and lymphatic vasculature. Afferent lymphatic vessels were detectable up to 30 minutes after injection with only minor contrast enhancement. Yet, the effect of early venous enhancement using contrast agents with extracellular distribution may significantly impair diagnostic quality of MRL. Our experience with Gd-DOTA-based MRL is in accordance with results of contrast-enhanced MRL performed in the clinical setting. Notohamiprodjo et al[32] described concomitant enhancement of veins and lymphatic vessels directly after contrast application in patients with lymphedema.

One limitation of this study consists in the rather long acquisition time of the high-resolution MRL sequences. Hence, the dynamics of AGuIX transport through the lymphatic system could not be investigated in detail. However, in comparison with Gd-labeled dendrimers, a faster transport of AGuIX through lymphatic capillaries and a shorter half-life in the lymphatic vasculature can be assumed. Analyses in a comparable setting demonstrated that the uptake of a 4-nm-sized nanoparticle fabricated by incubation of gadofosveset and human serum albumin peaks immediately after injection with subsequent drop-off.[33] In the present study, AGuIX performed better than Gd-DOTA with respect to immediate and sustained uptake into the popliteal lymph node. As a difference to dendrimer-based nanoparticles,[9] AGuIX was eliminated faster from the lymphatic system. The LN/muscle ratio calculation demonstrated washout from lymph nodes 60 minutes after intradermal administration. Decrease in SNR_{LNseg}, SNR_{LNmax}, and CNR_{LNmax} was observed 30 minutes after administration. When compared with gadofluorine-based MRL contrast agents,[12] testing of AGuIX indicated preferable pharmacokinetics with prolonged signal enhancement in the lymphatic vessels and lymph nodes.

It has to be emphasized that the herein presented MRL experiments were performed at a magnetic field strength of 9.4 T. High field strengths facilitate high spatial resolution and are particularly advantageous for small animal MRL. This is reflected by the high quality of lymphatic vessels depiction presented in this study. However, performing MRL at high field strengths is ambivalent. At lower field strengths between 1.5 T and 3 T, chemical shift- and susceptibility-related artifacts are less common than at the high field strengths utilized in most animal scanners. Furthermore, the physical properties of contrast media vary with the external magnetic field strength applied. For both contrast media employed in this experimental study, a negative correlation of r1 relaxivity with magnetic field strength has previously been reported.[20] Desirable gains in SNR due to the strong magnetic field employed may therefore be counteracted by impaired contrast media effectivity.

The induction of chronic hindlimb lymphedema in rodents is difficult and requires invasive lymphatic ablation.[34] In the present study, we combined radical popliteal and inguinal lymphadenectomy with subsequent irradiation. To mimic the lymphatic damage of clinical cancer treatment most precisely, we did not leave a skin gap, an otherwise popular experimental procedure in rodents for the prevention of spontaneous lymphatic reconnection.[35,36] Histopathological analyses 14 weeks after surgery revealed typical characteristics of chronic

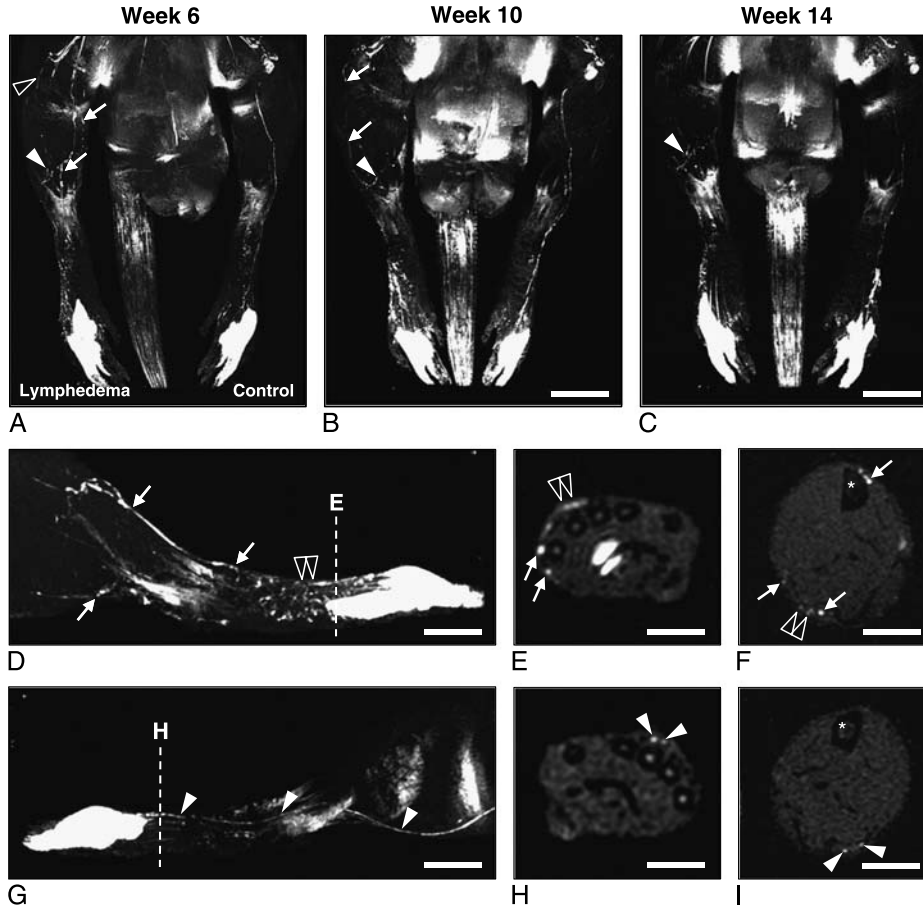

FIGURE 6. Repetitive AGuIX-based MRL after lymphedema induction. A, Lymphatic reorganization after 6 weeks with collateral lymphatic vessels (arrows). Lymphatic vessels bridging the defect site (arrowhead) toward the inguinal ligament (not shown). Ten (B) and 14 (C) weeks after lymphadenectomy, fewer collateral lymphatic vessels (arrows) are detectable. White arrowhead = ligated lymphatic vessels. Dorsolateral view of a lymphedematous (D) and control (G) hindlimb at week 6. D, Lymphatic network (double arrowhead) on the dorsum of the paw and collateral lymphatic vessels (arrows). Corresponding coronal sections of the paw (E) and 5 mm proximal of the distal tibiofibular joint (F). Dermal backflow around the ligated lymphatic vessels on the dorsum of the paw (E, double arrowhead) and less pronounced proximally (F, double arrowhead). Arrows = collateral lymphatic vessels. G–I, Regular configuration of the lymphatic vessels (arrowheads) in the control hindlimb. Asterisk in F and I = tibia. Scale bars: A–C = 9.5 mm, D and G = 7.5 mm, E and H = 3 mm, F and I = 5.5 mm.

lymphedema, such as tissue fibrosis, immune cell infiltration, and an increase in lymphatic vessel density and area. In addition, hindlimb volumes estimated by paw thickness measurements were elevated in the lymphedema group throughout the 14-week observation period. Moreover, AGuIX-based MRL 6, 10, and 14 weeks after lymphadenectomy revealed characteristic findings of lymphatic reorganization.

Comparable lymphatic reorganization after popliteal lymphadenectomy has been observed in mice using near-infrared fluorescence imaging.[37,38] One week after surgery, rupture of collateral lymphatic vessels with dermal backflow was reported. After 4 weeks, collateral pathways toward the inguinal lymph node were established and lymphatic vessels showed signs of maturation.[37] In our more invasive rat model, MRL 6 weeks after surgery demonstrated similar collateral lymph flow. Moreover, we observed residual dermal backflow close to the ligated lymphatic vessels. The newly visualized lymphatic vessels exhibited a greater variation in diameter when compared with nonoperated hindlimbs. Importantly, MRL-based analysis of lymphatic vessel maturation remains limited to morphological characterization. In contrast, near-infrared fluorescence imaging allows dynamic analyses, such as the assessment of lymphatic vessel contractility.[39]

Surprisingly, after 10 and 14 weeks, fewer collateral lymphatic vessels were detectable. This finding may indicate increased lymphangiogenesis-independent interstitial fluid drainage.[40] However, it remains unclear to what extent upstream interruption of the lymphatic pathway (ie, inguinal lymphadenectomy) or additional irradiation contributed to this phenomenon. Importantly, fibrosis has been shown to be a strong inhibitor of lymphatic regeneration.[41,42] Hence, we speculate that irradiation-induced tissue fibrosis was the major counterpart of lymphatic reorganization in the advanced stage of the herein investigated rodent lymphedema model.

Taken together, this study demonstrates that AGuIX-based MRL may be ideally suited for preclinical lymphatic imaging in rodents at high field. It yields sufficiently high spatial and temporal resolution for anatomical imaging of lymphatic vessels with diameters around 200 µm. Thus, AGuIX-based MRL may be a suitable tool to assess lymphatic regeneration after reconstructive lymphedema surgery, such as vascularized lymph node transfer[43] or lymphaticovenular anastomosis.[44] With shorter scan duration, high-resolution MRL could even be suitable to analyze lymphatic vessel function or lymphatic drainage, as already reported by other groups.[45] Moreover, AGuIX has been investigated in mouse models of lung cancer[16] and melanoma.[46] In both tumor types, restraint of the contrast agent in induced lesions has been observed 24 hours after application. This may pave the way for metastasis tracking after intradermal injection.

ACKNOWLEDGMENTS

The authors are grateful for the excellent technical assistance of Janine Becker, Caroline Bickelmann, Ruth Nickels, and Christina Körbel.

REFERENCES

1. Zhang F, Niu G, Lu G, et al. Preclinical lymphatic imaging. *Mol Imaging Biol*. 2011;13:599–612.
2. Sevick-Muraca EM, Kwon S, Rasmussen JC. Emerging lymphatic imaging technologies for mouse and man. *J Clin Invest*. 2014;124:905–914.
3. Leu AJ, Berk DA, Yuan F, et al. Flow velocity in the superficial lymphatic network of the mouse tail. *Am J Physiol*. 1994;267:H1507–H1513.
4. Misselwitz B, Platzek J, Radüchel B, et al. Gadofluorine 8: initial experience with a new contrast medium for interstitial MR lymphography. *MAGMA*. 1999;8:190–195.
5. Kobayashi H, Kawamoto S, Star RA, et al. Micro-magnetic resonance lymphangiography in mice using a novel dendrimer-based magnetic resonance imaging contrast agent. *Cancer Res*. 2003;63:271–276.
6. Kwon S, Sevick-Muraca EM. Noninvasive quantitative imaging of lymph function in mice. *Lymphat Res Biol*. 2007;5:219–231.
7. Proulx ST, Luciani P, Derzsi S, et al. Quantitative imaging of lymphatic function with liposomal indocyanine green. *Cancer Res*. 2010;70:7053–7062.
8. Kobayashi H, Kawamoto S, Brechbiel MW, et al. Detection of lymph node involvement in hematologic malignancies using micromagnetic resonance lymphangiography with a gadolinum-labeled dendrimer nanoparticle. *Neoplasia*. 2005;7:984–991.
9. Kobayashi H, Kawamoto S, Choyke PL, et al. Comparison of dendrimer-based macromolecular contrast agents for dynamic micro-magnetic resonance lymphangiography. *Magn Reson Med*. 2003;50:758–766.
10. Mounzer R, Shkarin P, Papademetris X, et al. Dynamic imaging of lymphatic vessels and lymph nodes using a bimodal nanoparticulate contrast agent. *Lymphat Res Biol*. 2007;5:151–158.
11. Fink C, Bock M, Kiessling F, et al. Interstitial magnetic resonance lymphography with gadobutrol in rats: evaluation of contrast kinetics. *Invest Radiol*. 2002;37:655–662.
12. Kiryu S, Inoue Y, Sheng F, et al. Interstitial MR lymphography in mice: comparative study with gadofluorine 8, gadofluorine M, and gadofluorine P. *Magn Reson Med Sci*. 2012;11:99–107.
13. Staatz G, Nolte-Ernsting CC, Adam GB, et al. Interstitial T1-weighted MR lymphography: lipophilic perfluorinated gadolinium chelates in pigs. *Radiology*. 2001;220:129–134.
14. Harika L, Weissleder R, Poss K, et al. MR lymphography with a lymphotropic T1-type MR contrast agent: Gd-DTPA-PGM. *Magn Reson Med*. 1995;33:88–92.
15. Sheng F, Inoue Y, Kiryu S, et al. Interstitial MR lymphography in mice with gadopentetate dimeglumine and gadoxetate disodium. *J Magn Reson Imaging*. 2011;33:490–497.
16. Lux F, Mignot A, Mowat P, et al. Ultrasmall rigid particles as multimodal probes for medical applications. *Angew Chem Int Ed Engl*. 2011;50:12299–12303.
17. Bianchi A, Dufort S, Lux F, et al. Targeting and in vivo imaging of non-small-cell lung cancer using nebulized multimodal contrast agents. *Proc Natl Acad Sci U S A*. 2014;111:9247–9252.
18. Sancey L, Lux F, Kotb S, et al. The use of theranostic gadolinium-based nanoprobes to improve radiotherapy efficacy. *Br J Radiol*. 2014;87:20140134.
19. Miladi I, Duc GL, Kryza D, et al. Biodistribution of ultra small gadolinium-based nanoparticles as theranostic agent: application to brain tumors. *J Biomater Appl*. 2013;28:385–394.
20. Fries P, Morr D, Müller A, et al. Evaluation of a gadolinium-based nanoparticle (AGuIX) for contrast-enhanced MRI of the liver in a rat model of hepatic colorectal cancer metastases at 9.4 tesla. *Rofo*. 2015;187:1108–1115.
21. Ruehm SG, Schroeder T, Debatin JF. Interstitial MR lymphography with a conventional extracellular gadolinium-based agent: assessment in rabbits. *Radiology*. 2001;218:664–669.
22. Herborn CU, Vogt FM, Lauenstein TC, et al. Assessment of normal, inflammatory, and tumor-bearing lymph nodes with contrast-enhanced interstitial magnetic resonance lymphography: preliminary results in rabbits. *J Magn Reson Imaging*. 2003;18:328–335.
23. Chwang WB, Jain R, Bagher-Ebadian H, et al. Measurement of rat brain tumor kinetics using an intravascular MR contrast agent and DCE-MRI nested model selection. *J Magn Reson Imaging*. 2014;40:1223–1229.
24. Yang CY, Nguyen DH, Wu CW, et al. Developing a lower limb lymphedema animal model with combined lymphadenectomy and low-dose radiation. *Plast Reconstr Surg Glob Open*. 2014;2:e121.
25. Frueh FS, Körbel C, Gassert L, et al. High-resolution 3D volumetry versus conventional measuring techniques for the assessment of experimental lymphedema in the mouse hindlimb. *Sci Rep*. 2016;6:34673.
26. Junqueira LC, Bignolas G, Brentani RR. Picrosirius staining plus polarization microscopy, a specific method for collagen detection in tissue sections. *Histochem J*. 1979;11:447–455.
27. Rasband WS. ImageJ, U. S. National Institutes of Health, Bethesda, Maryland, USA. 1997–2016. Available at: http://imagej.nih.gov/ij/.
28. R Core Team (2013). *R: A language and environment for statistical computing*. Vienna, Austria: R Foundation for Statistical Computing. ISBN 3-900051-07-0, URL. Available at: http://www.R-project.org/.
29. Harisinghani MG, Barentsz J, Hahn PF, et al. Noninvasive detection of clinically occult lymph-node metastases in prostate cancer. *N Engl J Med*. 2003;348:2491–2499. Erratum in: *N Engl J Med*. 2003;349:1010.
30. Heesakkers RA, Hövels AM, Jager GJ, et al. MRI with a lymph-node-specific contrast agent as an alternative to CT scan and lymph-node dissection in patients with prostate cancer: a prospective multicohort study. *Lancet Oncol*. 2008;9:850–856.
31. Lu Q, Delproposto Z, Hu A, et al. MR lymphography of lymphatic vessels in lower extremity with gynecologic oncology-related lymphedema. *PLoS One*. 2012;7:e50319.
32. Notohamiprodjo M, Weiss M, Baumeister RG, et al. MR lymphangiography at 3.0 T: correlation with lymphoscintigraphy. *Radiology*. 2012;264:78–87.
33. Nakajima T, Turkbey B, Sano K, et al. MR lymphangiography with intradermal gadofosveset and human serum albumin in mice and primates. *J Magn Reson Imaging*. 2014;40:691–697.
34. Frueh FS, Gousopoulos E, Rezaeian F, et al. Animal models in surgical lymphedema research—a systematic review. *J Surg Res*. 2016;200:208–220.
35. Oashi K, Furukawa H, Nishihara H, et al. Pathophysiological characteristics of melanoma in-transit metastasis in a lymphedema mouse model. *J Invest Dermatol*. 2013;133:537–544.
36. Bramos A, Perrault D, Yang S, et al. Prevention of postsurgical lymphedema by 9-cis retinoic acid. *Ann Surg*. 2016;264:353–361.
37. Blum KS, Proulx ST, Luciani P, et al. Dynamics of lymphatic regeneration and flow patterns after lymph node dissection. *Breast Cancer Res Treat*. 2013;139:81–86.
38. Kwon S, Agollah GD, Wu G, et al. Spatio-temporal changes of lymphatic contractility and drainage patterns following lymphadenectomy in mice. *PLoS One*. 2014;9:e106034.
39. Gousopoulos E, Proulx ST, Scholl J, et al. Prominent lymphatic vessel hyperplasia with progressive dysfunction and distinct immune cell infiltration in lymphedema. *Am J Pathol*. 2016;186:2193–2203.
40. Ongstad EL, Bouta EM, Roberts JE, et al. Lymphangiogenesis-independent resolution of experimental edema. *Am J Physiol Heart Circ Physiol*. 2010;299:H46–H54.
41. Avraham T, Clavin NW, Daluvoy SV, et al. Fibrosis is a key inhibitor of lymphatic regeneration. *Plast Reconstr Surg*. 2009;124:438–450.
42. Avraham T, Yan A, Zampell JC, et al. Radiation therapy causes loss of dermal lymphatic vessels and interferes with lymphatic function by TGF-beta1-mediated tissue fibrosis. *Am J Physiol Cell Physiol*. 2010;299:C589–C605.
43. Cheng MH, Huang JJ, Wu CW, et al. The mechanism of vascularized lymph node transfer for lymphedema: natural lymphaticovenous drainage. *Plast Reconstr Surg*. 2014;133:192e–198e.
44. Yamamoto T, Yamamoto N, Yamashita M, et al. Establishment of supermicrosurgical lymphaticovenular anastomosis model in rat. *Microsurgery*. 2017;37:57–60.
45. Pan D, Suzuki Y, Yang PC, et al. Indirect magnetic resonance lymphangiography to assess lymphatic function in experimental murine lymphedema. *Lymphat Res Biol*. 2006;4:211–216.
46. Kotb S, Detappe A, Lux F, et al. Gadolinium-based nanoparticles and radiation therapy for multiple brain melanoma metastases: proof of concept before phase I trial. *Theranostics*. 2016;6:418–427.